Journal of Materials Research and Technology 41 (2026) 2523–2533

Contents lists available at ScienceDirect

Journal of Materials Research and Technology

journal homepage: www.elsevier.com/locate/jmrt

Dry sliding wear behavior of laser powder bed fusion processed Inconel 718 alloy

Zhengxi Hu [a,*], Zhan Wen Chen [b]

[a] Faculty of Artificial Intelligence, Hezhou University, Hezhou City, Guangxi, China
[b] Department of Mechanical Engineering, Auckland University of Technology, Auckland, New Zealand

ARTICLE INFO

Keywords:
Inconel 718 alloy
LPBF
Microstructural characteristics
Tribology
Wear

ABSTRACT

With the increasing adoption of laser powder bed fusion (LPBF) for fabricating Inconel 718 alloys, growing attention has been directed toward evaluating their operational performance, particularly in relation to mechanical properties, fatigue behavior, and tribological characteristics. In the present study, dry linear reciprocating sliding wear tests were conducted to compare the wear behavior of LPBF-processed Inconel 718 with that of conventionally processed (CP) Inconel 718. The experiments were performed under different test conditions using Al_2O_3 balls as the counter body. The results indicate that, for both CP and LPBF alloys, the wear rate increases with applied load. However, the wear rate does not necessarily increase with frequency, and no clear positive correlation was observed. Moreover, the LPBF Inconel 718 alloy exhibited a little higher wear rate than its CP counterpart, a difference primarily attributed to variations in internal microstructural characteristics.

1. Introduction

Inconel 718 is widely employed in aerospace, power generation, automotive, and other industries owing to its excellent high-temperature strength, corrosion resistance, and weldability [1–3]. Nevertheless, the complex fabrication process and high production cost of this nickel-based superalloy remain critical bottlenecks limiting its broader application [4]. For instance, turbine blades with intricate internal cooling channels for jet engines are typically produced through precision casting. In this process, a wax model is first used to prepare a ceramic mold, into which a large volume of molten superalloy is vacuum-cast. The entire cycle is time-consuming, involving homogenization treatments at temperatures near the alloy's melting point [5]. In addition, conventional manufacturing routes such as investment casting, forging, and machining are often accompanied by severe chemical segregation, low material utilization, and yields typically below 50 % [6].

As an advanced additive manufacturing technique, laser powder bed fusion (LPBF) enables the fabrication of complex geometries with near-net-shape precision, making it highly attractive for lightweight, high-performance components [7]. Previous studies have demonstrated that laser energy density strongly influences the microstructure, mechanical performance, and distortion behavior of LPBF-processed Inconel 718 [8, 9]. For example, within the range of 0.1–0.3 J/mm, an energy density of 0.2 J/mm was reported to yield the lowest porosity and optimal mechanical properties, including a yield strength of 775 MPa, tensile strength of 1055 MPa, and elongation of 29.5 %.

Hilaire et al. [10] further reported that variations in laser processing parameters affect defect morphology and melt-pool geometry even when relative density exceeds 99.5 %. Fracture surface analysis revealed inter-dendritic, intergranular, and inter-melt-pool modes, with inter-dendritic cracking attributed to localized stress and brittle Laves phase precipitation. Notably, internal gas porosity cannot be entirely eliminated through parameter optimization. Consistently, LPBF Inconel 718 exhibits characteristic microstructural features such as interdendritic phases and processing-induced defects, which serve as preferential crack initiation sites [11]. Although the presence of δ phase does not significantly alter axial fatigue behavior compared with wrought data, it reduces impact toughness due to crack propagation along δ-decorated grain boundaries [12]. Post-processing heat treatments have been shown to substantially enhance hardness, tensile strength, and fatigue limits by up to 46 %, 41 %, and 27 %, respectively [13].

A broad body of literature has explored the microstructure and mechanical properties of Ni-based superalloys [14–29]. For example, Deng et al. [30] observed that as-built LPBF Inconel 718 develops a fine cellular-dendritic microstructure, with Laves phases precipitating in

* Corresponding author.
E-mail address: huzhengxi588193@126.com (Z. Hu).

https://doi.org/10.1016/j.jmrt.2026.01.122
Received 8 December 2025; Received in revised form 14 January 2026; Accepted 15 January 2026
Available online 16 January 2026

interdendritic regions. EBSD analysis revealed relatively weak textures in both vertical and horizontal builds. Vertically built samples exhibited lower tensile strength but higher ductility compared with horizontally built counterparts, an effect linked to both crystallographic orientation and differences in residual stress and dislocation density. Heat treatment increased strength but reduced ductility, with the strength disparity between vertical and horizontal builds diminishing at elevated treatment temperatures due to stress relaxation and defect annihilation. In general, AM-induced defects such as porosity and high residual stresses compromise the mechanical integrity of LPBF Inconel 718, while optimized processing and heat treatment can effectively mitigate these shortcomings [31].

Tribological investigations further highlight the complexity of wear mechanisms in Inconel 718. For instance, studies of laser-cladded coatings reveal a transition from mixed slip to gross slip regimes with increasing temperature, where oxidation, abrasion, fatigue, and adhesion dominate the wear process [32]. Zahoor et al. [33] demonstrated that sliding contact with stainless steel promotes the formation of a tribological layer, with the prevailing wear mechanism dependent on the counterface material. The article indicates that at a testing frequency of 15 Hz, the lowest wear rate occurs at a normal load of 30 N, whereas the highest wear rates are observed at 10 N and 50 N. Nevertheless, the dependence of wear rate on load at other operating frequencies was not explored. Moreover, the engineering relevance of maintaining a constant operating frequency of 15 Hz appears to be limited in practical applications, which raises concerns regarding the generality of the conclusions.

To address this gap, the present study conducted dry sliding wear experiments to directly compare the tribological behavior of conventionally processed Inconel718 alloy and 718 samples fabricated by laser powder bed fusion (LPBF) without subsequent heat treatment. The effects of normal load and sliding frequency on the wear rate, coefficient of friction (COF), and worn surface morphology were systematically investigated. The results aim to clarify the influence of load and frequency on wear behavior and to elucidate the roles of processing route and microstructural characteristics in governing the dry sliding wear resistance of Inconel 718 alloy.

2. Experimental procedures

Additively manufactured samples of Inconel 718 alloy were made using a LPBF machine (AM400, built by Renishaw, UK) Optimized parameters were used during the LPBF process as follows: the laser power of 190 W, scanning speed of 600 mm/s, hatch space of 0.04 mm, layer thickness of 0.03 mm, layer incremental orientation angle of 67.5°. The Inconel 718 alloy powder used in LPBF is gas-atomized with particle size distribution ranging from 10 to 48 μm as shown in Fig. 1(a) and its chemical composition is presented in Fig. 1(b).

These samples were produced using machine parameters normally for achieving nearly fully dense parts. (Hereinafter referred to as LP samples). The conventionally processed Inconel 718 alloy sheet was obtained from supplier (Shenzhen Qiyi Metal Materials Co., Ltd. China). PM-HIP 718 alloy further processed by hot rolling, conforming to ASTM B670 (Hereinafter referred to as CP samples).

All the samples were made or sectioned into 40 mm × 20 mm x 5 mm in size for the samples to be perfectly fit into the sample holder of the wear tester. All wear samples were ground by SiC grinding papers until grit-2400 to achieve an average surface roughness (Ra) of 0.05 μm measured using a Taylor Hobson Talysurf 2D-profilometer (see Fig. 2).

The metallographic etchant consisted of 5g $CuCl_2$, 100 mL HCl, and 100 mL C_2H_5OH. The etching time was 30 s. After etching, the samples were immediately rinsed with clean water, dehydrated with absolute ethanol, and then rapidly dried using cold air.

Hardness tests were conducted on these polished samples using a Leco LM-800AT microhardness tester using a load of 1 kgf. Hardness values were determined to be 270 ± 20Hv for CP samples, 290 ± 20Hv for LP samples, based on 10 measurements for each type of samples. A commercial Linear Reciprocating Tribometer (Ducom TR-282, USA) was used and ball on plate was selected to conduct the dry sliding wear tests. Coefficient of friction (COF) was automatically given by the device. Tests were conducted using a range of test conditions, as listed in Table 1. Duplicate tests were conducted for each condition. The counter ball material was Al_2O_3 and the ball diameter was 10 mm. A 40 mm × 20 mm x 5 mm sample was used for multiple tests but each wear track was sufficiently spaced. After testing, wear volume was estimated. This was done by first determining 5 cross sectional profiles along each wear track using a stylus profilometer. The cross-sectional profiles were then converted to cross sectional areas using ImageJ software. The average value of these areas was then multiplied by the track length to yield the wear volume of the track. The conventionally used wear rate (Wr) is then taken as the wear volume divided by the sliding distance (480 m), and the ambient environment is room temperature. The wear rate was

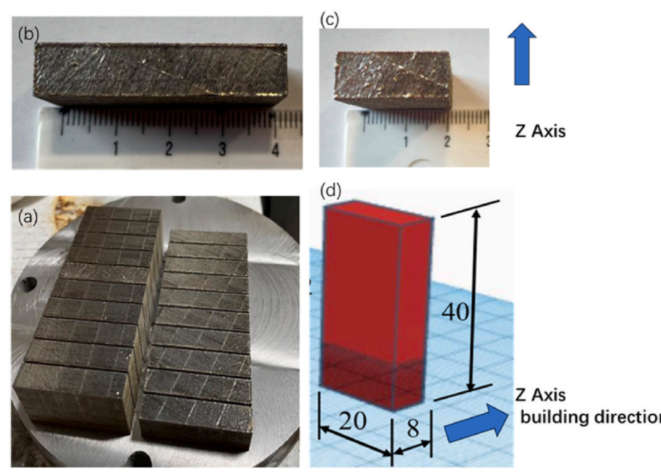

Fig. 2. LPBF sample shape and building direction.

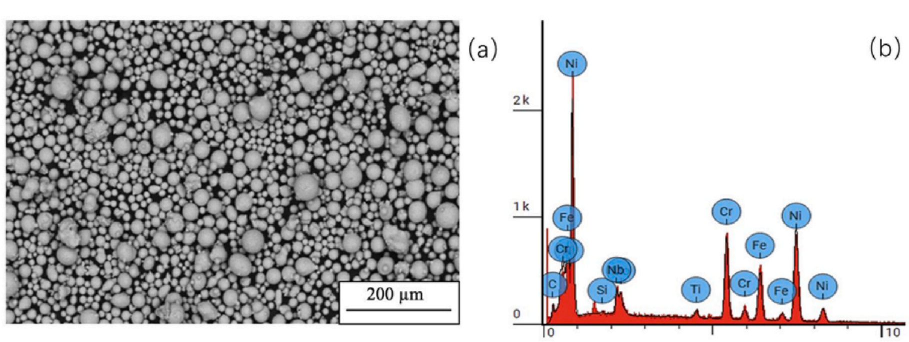

Fig. 1. (a) particle size distribution and (b) chemical composition of the 718 powders.

Table 1
Sliding wear conditions.

Loads (F_N)	10 N	15 N	20 N
Frequency (f)	2 Hz	5 Hz	8 Hz
Sliding stroke	10 mm		
Sliding distance (cycle)	480 m	(thus 24,000 cycles)	

calculated using the equation as follows:

$$Wr = \Delta S*M/L \tag{1}$$

where Wr is the wear rate (mm^3/m), ΔS is the average value of these areas of the tracks (mm^2), M is the sliding stroke(10 mm). L is the sliding distance (480 m).

After testing and measuring, wear tracks were examined using a

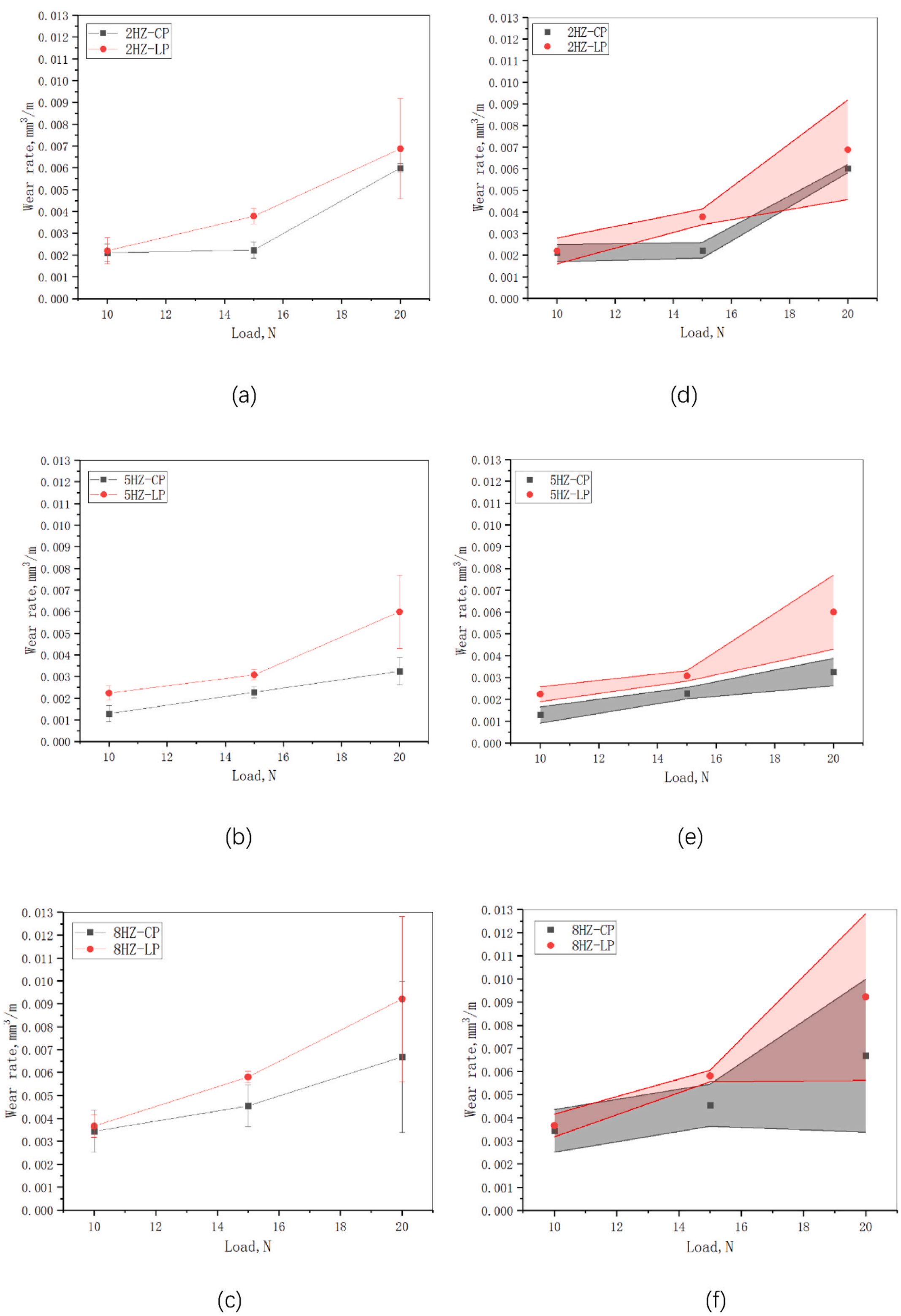

Fig. 3. Wr values vs. load at different frequence of 2Hz(a), 5Hz(b), 8Hz(c).

Hitachi SU-70 field emission scanning electron microscope (FE-SEM) with X-ray energy dispersive spectroscopy (EDS).

3. Results

3.1. Tribological properties

Under constant frequencies of 2 Hz, 5 Hz and 8 Hz, the wear rates of both LP materials and CP materials increased with the increase in load, exhibiting typical load-sensitive wear behavior. As the load increased from 10 N to 20 N, the wear rates of both materials significantly rose, indicating that a higher normal load would result in greater contact stress and a more intense wear reaction, as shown in Fig. 3.

It is worth noting that under the same load conditions, the wear rate of LP material is a little higher than that of CP material, and the difference becomes more significant in the high load range. As shown in Fig. 3 (c), Especially at 20 N conditions, the wear rate of LP is close to 0.0092 mm^3/m, which is much higher than that of CP at around 0.0069 mm^3/m. Although these average wear rates vary with different loads, the error range under different conditions significantly overlap, indicating that these differences are not statistically significant. This suggests that under the current testing conditions, the load itself does not dominate the wear behavior. From a mechanistic perspective, the increase in contact temperature under higher loads may promote surface oxidation, while the enhanced debris generation can change the contact state through the third-body effect. The competition among these mechanisms may result in comparable wear rates and overlapping error ranges under different loads.

Fig. 4(a) shows that the wear rate keeps increasing as the load increases, Fig. 4(b) is observed the lack of a clear correlation between wear rate and frequency, it attributed to several interacting mechanisms. At higher frequencies, the contact temperature at the sliding interface tends to increase, which can promote the formation of a thin oxide layer that temporarily protects the surface and reduces direct metal-to-metal contact. Additionally, wear debris generated during sliding can accumulate in the contact zone, forming a third-body layer that alters the effective contact conditions and further instigates wear. These competing effects—temperature-induced oxidation and debris-mediated—can lead to a non-monotonic relationship between frequency and wear rate, explaining the absence of a simple linear trend in our results. Similar phenomena have been observed in previous studies on Ti–6Al–4V alloy [34] (see Fig. 5).

To further understand the influence of frequency on tribological behavior, the coefficient of friction (COF) evolution of LP and CP materials was compared under a constant load of 15 N at frequencies of 2 Hz, 5 Hz, and 8 Hz.

At the lowest frequency of 2 Hz, the LP material rapidly reached a stable COF (0.72) with minimal fluctuation, whereas the CP material started with a low COF and exhibited a sharp increase at around 200 s, eventually stabilizing near 0.78.

When the frequency increased to 5 Hz, both materials showed faster stabilization. The LP material maintained a high COF (0.85), while the CP material reached a relatively lower COF (0.75) with improved stability compared to the 2 Hz condition. This indicates that moderate frequency enhances tribo-film formation and improves frictional consistency, especially for CP sample.

At the highest frequency of 8 Hz, both materials exhibited further increased COF (0.96 for LP and 0.79 for CP). The high frequency likely introduced more energy input at the interface, promoting thermal effects and debris accumulation, which led to higher frictional resistance.

COF of LP sample remained higher across all frequencies, possibly due to microstructural inhomogeneity, weak oxide layer formation, or unstable tribo-layer characteristics. Increasing frequency leads to faster friction stabilization and higher steady-state COFs for both materials, while LP sample consistently shows higher COF, implying greater interfacial resistance and potential for increased wear under a higher load. COFs after 300 s are not shown in the figures, which is due to the residual wear debris in the subsequent friction process, oxidation and other factors that affect COF.

As shown in Fig. 6, there are significant differences in the widths of the track of CP and LP samples under different loads and frequencies.

As shown in Fig. 6(a) and (b), the track width increases with increasing applied load for both conditions, which is consistent with the classical understanding that higher contact forces promote more severe material removal. However, distinct differences can be observed between CP and LP samples. At lower load (10 N), the CP specimens exhibit narrower wear tracks, particularly at 5 Hz, suggesting superior resistance to wear compared with LP. At intermediate load (15 N), the frequency effect becomes more pronounced, with 8 Hz producing significantly wider tracks under both conditions, whereas CP samples still maintain relatively smaller widths at 2 Hz and 5 Hz. At higher load (20 N), the difference between CP and LP diminishes, and the wear track widths converge, indicating that the beneficial effect of CP samples weakens under heavy loading. Overall, the results demonstrate that CP samples are more effective in mitigating wear at low to intermediate loads, whereas the advantage disappears when the load is sufficiently high.

Moreover, wear sensitivity to frequency is observed under both

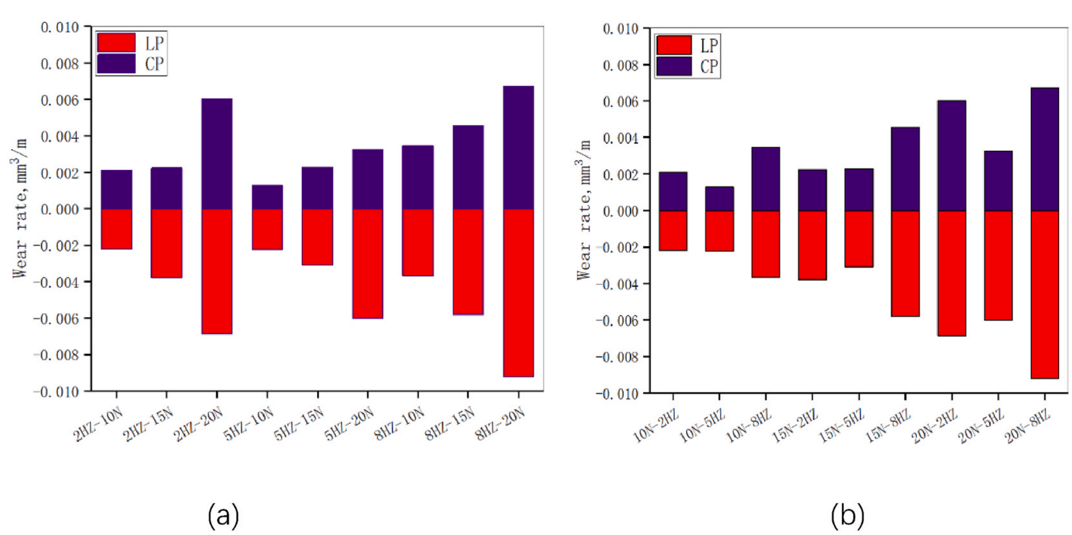

Fig. 4. Wr value without error bars vs. test load (a) and test frequency (b).

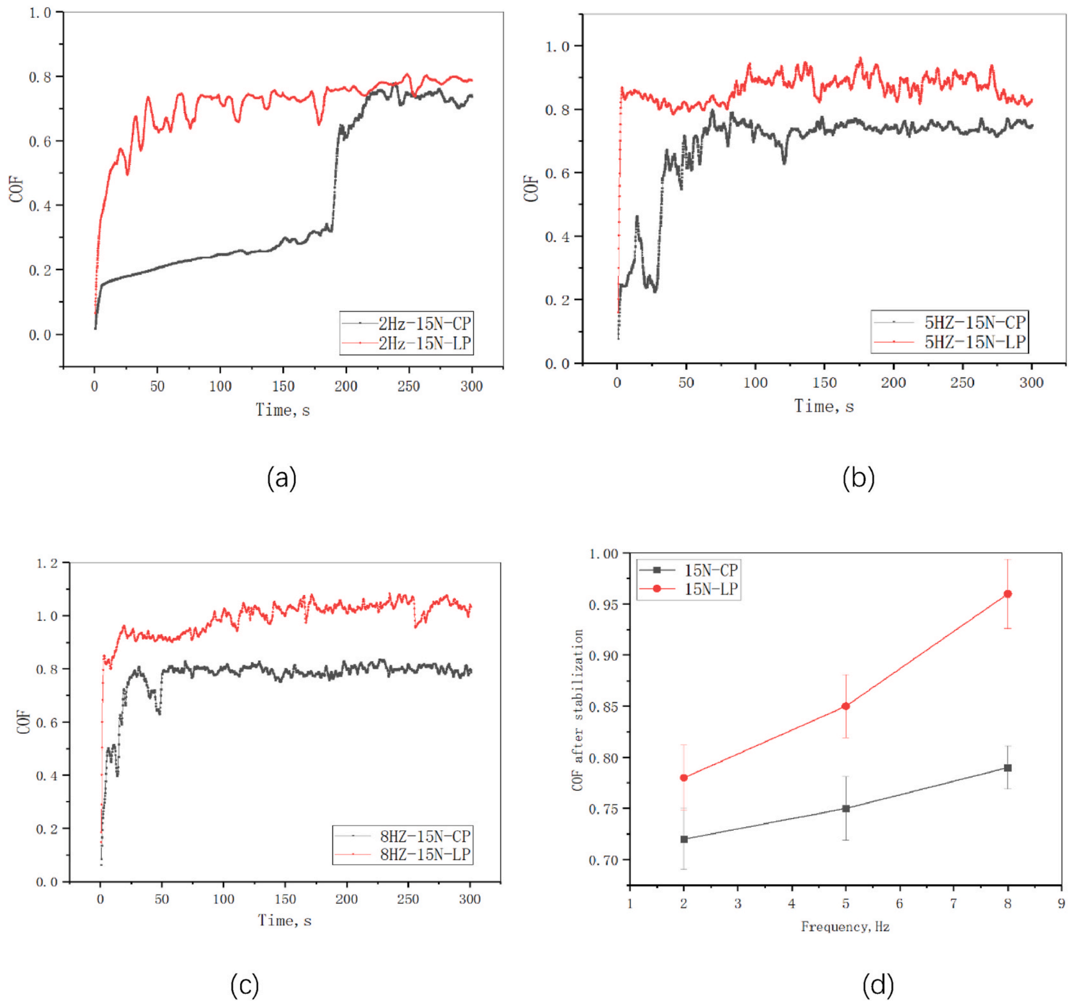

Fig. 5. COF values vs. the time in the first 300 s at 15 N load for different frequence: (a) 2Hz, (b) 5Hz, (c) 8Hz and (d)COF after stabilization.

conditions, with higher frequency (8 Hz) consistently associated with larger wear track widths, which can be seen from Fig. 6(c) and (d), the increased error bars at 8 Hz, particularly under 20 N, suggest higher variability in wear response, possibly due to localized temperature effects or unstable contact conditions. the results indicate that both load and frequency interactively influence the wear performance, with frequency having a nonlinear impact at higher loads.

3.2. Worn surface morphology

Fig. 7 presents the SEM images (200 ×) of worn surfaces for CP and LP materials, respectively, under identical wear conditions. In Fig. 7(a)–(c) (e), the CP sample exhibits well-aligned grooves parallel to the wear direction, indicating dominant shear-induced plastic deformation during sliding. The surface appears relatively smooth, with signs of material tearing or delamination, suggesting a stable abrasive wear mechanism.

In contrast, the LP sample Fig. 7(b)–(d) (f) show significantly rougher surface, with diminished directional wear features and the presence of irregular particles, debris accumulation, and surface protrusions. This morphology implies a more complex wear process involving not only plastic flow but also localized brittle fracture and potential thermal effects. Some regions exhibit melted-and-re-solidified textures, likely attributed to microstructural changes induced by laser powder bed fusion processing, which may have altered the wear resistance and response of the surface layer.

LP material, revealing severe surface fragmentation and large-scale debris. The appearance of plate-like debris and re-solidified remnants suggests that under extended or high-load conditions, the LP surface layer may undergo crack initiation and propagation due to brittleness or residual thermal stresses, leading to a wear mechanism dominated by spalling and material removal.

CP material tends to experience stable, plasticity-controlled wear, while LP material exhibits a more aggressive wear behavior involving a combination of plastic flow, cracking, and thermal-induced fragmentation, resulting in more severe surface degradation.

The images from the high magnification SEM clearly show the obvious damage features on the surface, which highlight different wear mechanisms. In Fig. 8(a) and(b), a significant pit appears on the surface. Under the action of external load, due to the interatomic bonding, local connection points will form at the contact points of the micro-convexities on the surface. With the continuous relative motion, these connection points will bear shear stress, which may exceed the cohesive strength of the material. Therefore, the material on one surface may transfer to another surface or be completely stripped by the abrasive material, forming a typical adhesive wear mechanism (see Fig. 9).

As for Fig. 8(a), next to the pit, there are multiple micro-cracks extending in different directions. These cracks indicate fatigue damage caused by stress, which may be exacerbated by repeated mechanical loading or thermal cycling, thereby accelerating the generation and expansion of cracks starting from the edge of the pit. Morphology indicates that the main wear mechanism is driven by mechanical stress and material layering.

In contrast, in Fig. 8(b), a clear pit is also shown, but no cracks are present. Instead, many small holes can be observed on the entire surface,

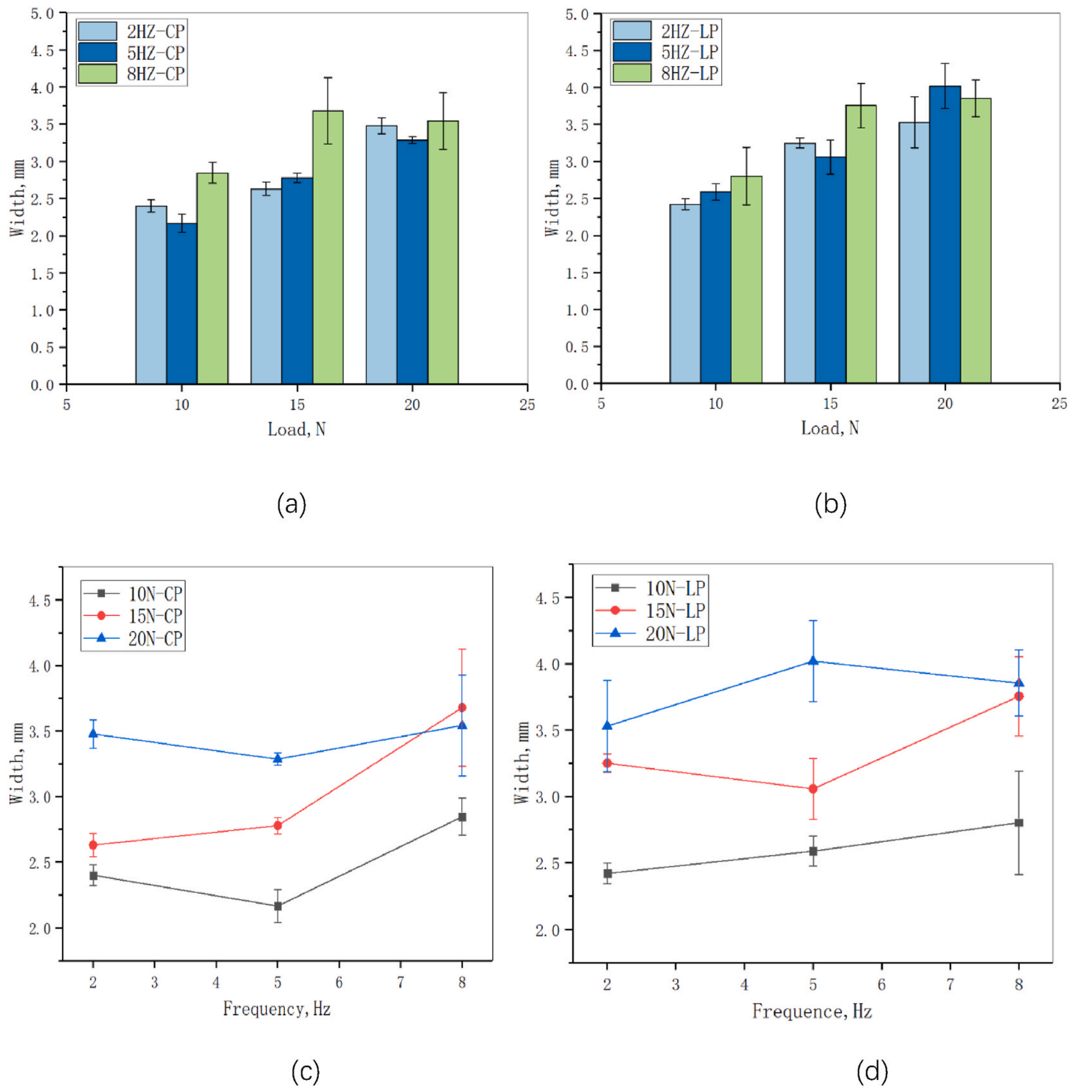

Fig. 6. Average measured width and standard deviation values plotted as a function of (a,b) test load and (c,d) test frequency.

especially near the pit area. These pores may be due to the retention of gas during the processing of the LP sample or the uneven microstructure. During the LPBF processing, because of the high energy density heating and sudden cooling, the material contracts and thus forms voids. Unlike the image in Fig. 8(a), the formation of cracks is more widespread in the first image, while the damage here seems to be related to material pores. The presence of pores may weaken the integrity of the structure, accelerate the wear of the material [10], and exhibit a higher wear rate, in addition to presenting the typical adhesive wear, and showing the defects of the structure itself.

Although both images show adhesive wear, the main degradation patterns are different: the first mode is characterized by crack-assisted mechanical wear, while the second mode is possibly related to pores. This contrast highlights the importance of underlying microscopic structural features that play a key role in the evolution of material wear, such as residual stress, pore size and distribution, etc.

3.3. Mechanism and discussion

During the wear process, both the surface layer and sub-surface layer undergo plastic deformation. Under repeated cyclic loading, strain accumulates on the surface and sub-surface of the specimen, leading to the formation of furrows as the primary manifestation of wear. Under the influence of cyclic loading induced by the applied load, cracks initiate and propagate within the wear layer, ultimately resulting in the detachment of wear debris. The mechanical properties of the material, including hardness, toughness, and work hardening behavior, significantly influence the extent of abrasive wear [35–37].

When the specimen undergoes abrasive wear, abrasive particles are pressed into the wear surface under compressive stress and displaced forward under shear stress, thereby forming furrows. Simultaneously, cutting action generates wear debris that separates from the surface. If the wear layer exhibits good plasticity, abrasive particles create furrows by displacing the worn material to the sides and front of the groove. The material on the furrow edges experiences severe plastic deformation, leading to delamination. A portion of the wear debris detaches from the surface, while another accumulates on the sides and front of the furrow due to the intense plastic deformation, contributing to the generation of wear debris. Certain microscopic asperities come into real contact, resulting in localized bonding between the two surfaces. During relative motion, these cold-welded regions are sheared apart, and during this tearing process, material may transfer from one surface to the other or be directly removed, leading to adhesive wear as seen in Fig. 8.

Both CP and LP materials exhibit minor oxidation as evidenced by EDS analysis, possibly formed by oxidation due to localized flash temperatures during friction [38]. The porous surface of LP sample increases the chance of contact with oxygen, thereby leading to more oxidation, as shows in Tables 2 and 3.

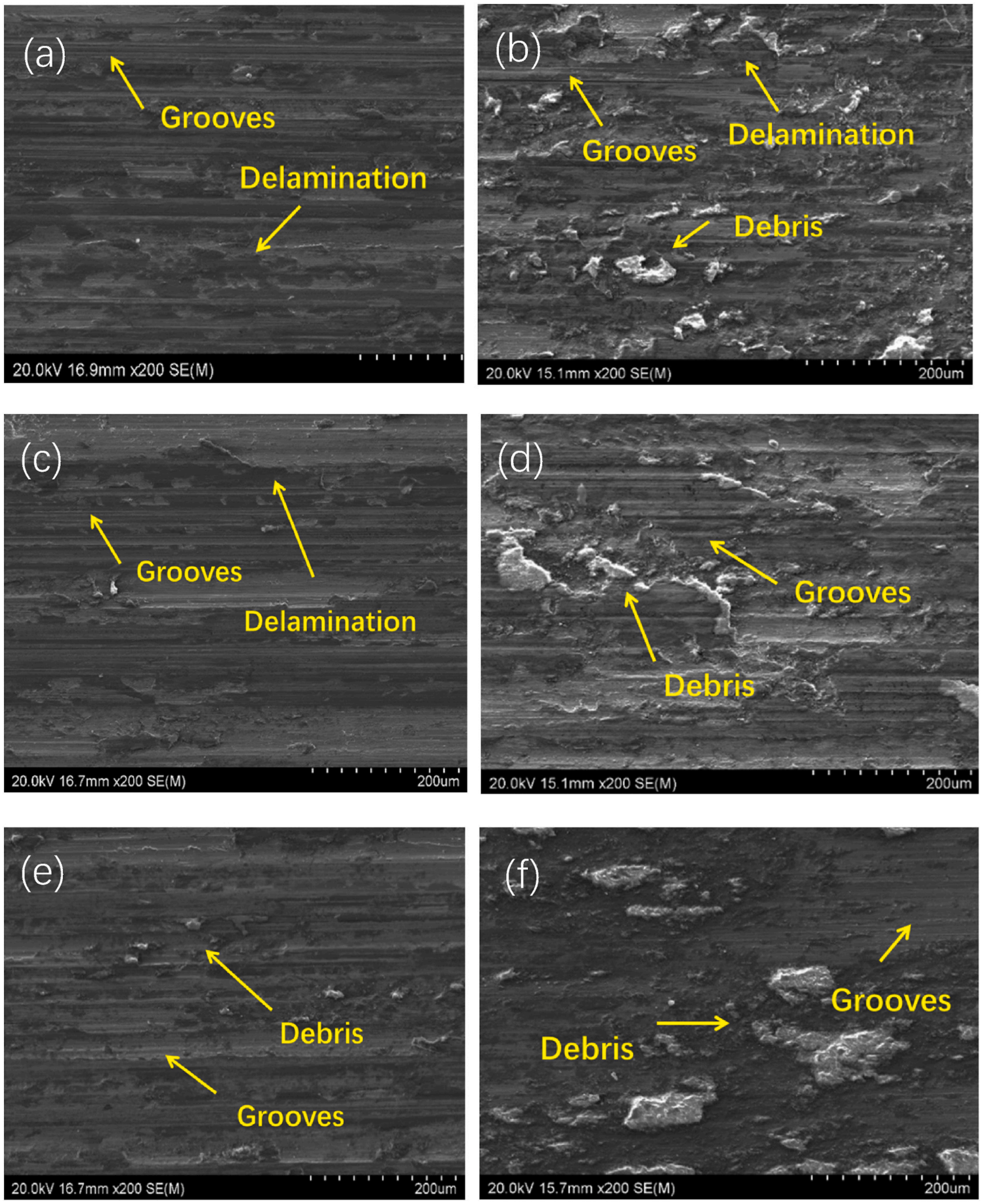

Fig. 7. Comparison of SEM images of CP and LP materials at 5Hz under different Loads (a) and (b)10 N; (c) and (d)15 N; (e) and (f)20 N.

In the case of the CP sample, fatigue wear cracks form on both the surface and sub-surface under cyclic loading, as illustrated in Fig. 8(a). Fatigue crack initiation is typically preceded by a latent period. In the early stages of wear, the surface undergoes work hardening due to plastic deformation without the formation of micro-cracks, and the sub-surface remains largely unaffected. With continued cyclic loading, cracks begin to nucleate and propagate under the influence of the friction pair. If the applied load exceeds the material's fatigue limit, fatigue spalling may occur; however, this phenomenon was not observed in the current experiment, likely due to the limited duration of the friction process.

For LP materials, a greater amount of wear debris is generated during the friction process, indicating a higher prevalence of both abrasion and adhesion wear mechanisms. The presence of crystalline defects along the build direction, as observed in SEM images Fig. 8(b), contributes to an increased wear rate. Higher hardness and thus higher strength of the alloy has resulted in a litter deformation zone, and lower ductility of the LP 718 alloy allows has a higher amount of fracture and wear loss as well [34].

Existing literatures indicate that after hot rolling, the surface and central regions of the 718 alloy exhibit differences in microstructure and mechanical properties [39,40] (see Fig. 10). The surface, subjected to higher deformation and faster cooling, tends to have finer grains, whereas the center, experiencing relatively lower deformation and slower cooling, develops slightly coarser grains. Some literatures have studied the crystal size and structural orientation of the heat rolling processed 718 alloy [41,42], the microstructure of the alloy is dominated by equiaxed grains [43], it should be noted that in this paper, the sliding direction of dry friction is consistent with the hot rolling direction as showed in Fig. 11(a). To make the expression more vivid, the grain size of the surface and the center parts of the material of CP 718 have been marked, in fact, this distinction does not exist because the

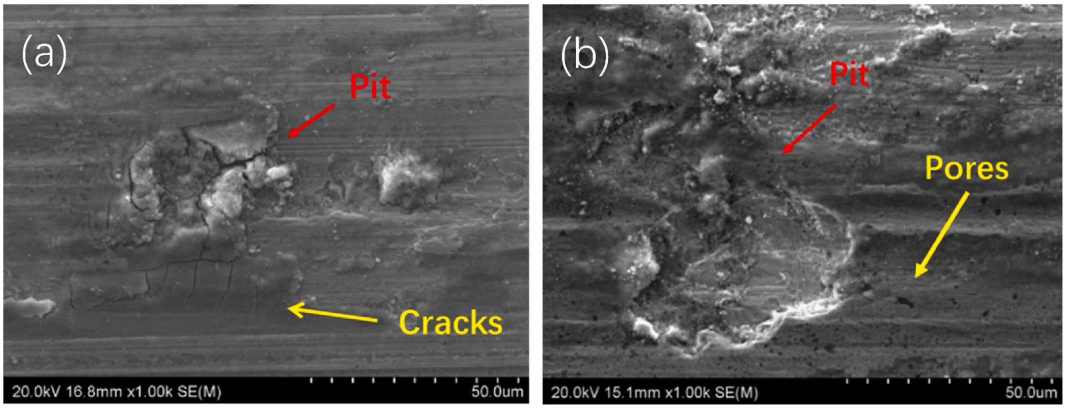

Fig. 8. High magnification SEM images of CP (a) and LP(*b*)samples at 5HZ under15 N.

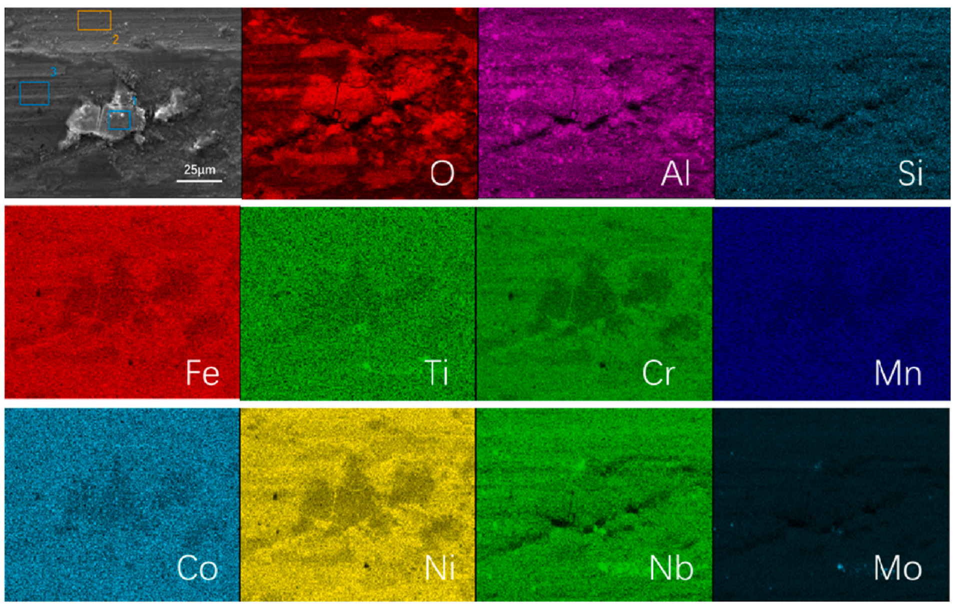

Fig. 9. SEM images of the CP sample worn surface with EDS map at 15 N and 5HZ.

Table 2
Weight % in different area of CP sample.

	O	Al	Si	Ti	Cr	Mn	Fe	Co	Ni	Nb	Mo
1	13.03	3.64	0.12	0.71	15.76	0.08	16.31	0.05	43.21	4.73	2.35
2	0.00	0.71	0.13	0.84	18.77	0.00	19.59	0.03	51.91	5.30	2.71
3	28.78	2.35	0.07	0.57	11.42	0.07	19.92	0.01	32.15	3.42	0.86

surface of the material has been removed. Fig. 11(b) indicates that the sliding direction is perpendicular to the build direction of the LP material.

However, in LP 718 specimens, it is possible to observe the typical columnar grains along the build direction (Z) with rod elongated shaped grains, in XZ and YZ planes, it is possible to observe equiaxed grains [8], these chips form flocculent structures under the cyclic loads, which might be related to the detachment of columnar crystals.

The wear rate of LP sample is highest when the wear direction is perpendicular to the build direction, as illustrated in Table 4, Anandakrishnan V [44] pointed out that the load is the major factor, which predominantly influenced the wear rate, followed by the sliding speed and the built direction. Different build directions will lead to differences in mechanical properties, orientation dependence of mechanical

Table 3
Weight % in different area of LP sample.

	O	Al	Si	Ti	Cr	Mn	Fe	Co	Ni	Nb	Mo
1	26.60	2.40	0.10	0.76	12.68	0.16	13.52	0.14	37.07	4.43	2.14
2	0.00	0.57	0.11	0.99	18.02	0.00	18.73	0.04	52.74	5.98	2.81
3	32.11	2.41	0.07	0.55	12.08	0.11	12.32	0.00	34.52	3.87	1.96

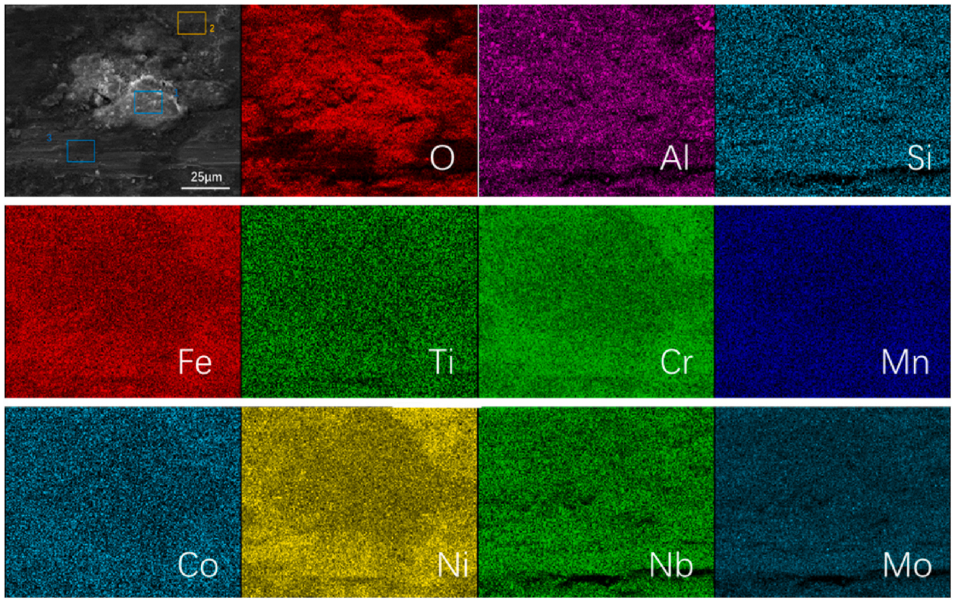

Fig. 10. SEM images of the LP sample worn surface with EDS map at 15 N and 5HZ.

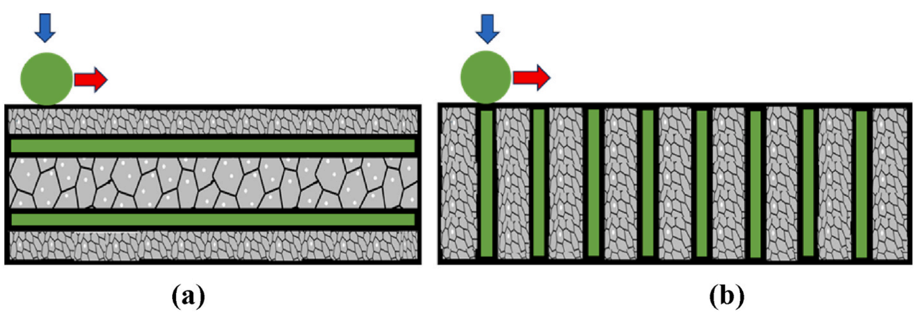

Fig. 11. schematic diagram showing the difference in wear rate in CP(a) and LP(b) materials.

Table 4
Build direction effect vs. wear rate of LP sample from literature [44].

S. No.	Load (N)	Build orientation (Deg)	Sliding velocity(m/s)	Wear rate (mm^3/m)	S/N ratio
1	10	0	1	0.0003963	68.0393
2	10	45	2	0.0003249	69.7662
3	10	90	3	0.0009942	60.0507
4	20	0	2	0.0008913	60.9999
5	20	45	3	0.0010967	59.1979
6	20	90	1	0.0009944	60.0486
7	30	0	3	0.0019456	54.2188
8	30	45	1	0.0012667	57.9462
9	30	90	2	0.0018022	54.8840

properties of the as-manufactured LP 718 are mainly attributed to the different amount of residual stress and dislocations accumulated in the cellular-dendrite [16], as showed in Table 5.

Table 5
Built direction vs. mechanical properties of LPBF 718 from literature [16].

Build direction	Yield strength (MP)	Ultimate tensile strength (MP)	elongation (%)
Horizontally built	790	1080	31
Vertically built	610	990	36

However, study on the Wear of LPBF processed 316 Stainless Steel shows that COF and wear rate seems not to be influenced much by build direction [45], which shows uncertainty of build direction on wear loss. Since investigating the effects of build direction on the wear rate of LP material is out of the scope of the present study, future work on exploring the exact effects on LP 718 alloy of tailoring texture is needed. After hot rolling, there will be no obvious columnar crystals in CP material, since the columnar crystals in the as-cast state will be broken and transformed into recrystallized equiaxed crystals as we have mentioned above, however, the LP material that has not undergone any heat treatment is more prone to detachment under the action of frictional shear force due to defects and dislocations on the columnar crystals or dendritic crystals.

To better reveal the internal microstructural features of the material, the samples were subjected to etching. After metallographic etching, the microstructures were examined using a scanning electron microscope at a magnification of 3000 × , as showed in Fig. 12.

The LP 718 alloy exhibits pronounced preferentially etched bands with a strong directional feature, indicating a higher degree of microstructural heterogeneity. In contrast, the CP 718 alloy shows a more homogeneous etching response, suggesting a finer and more uniform microstructure.

Although fabricating Inconel 718 alloys by LPBF with exceptional wear resistance directly presents considerable challenges, it remains a promising and exciting area of ongoing research.

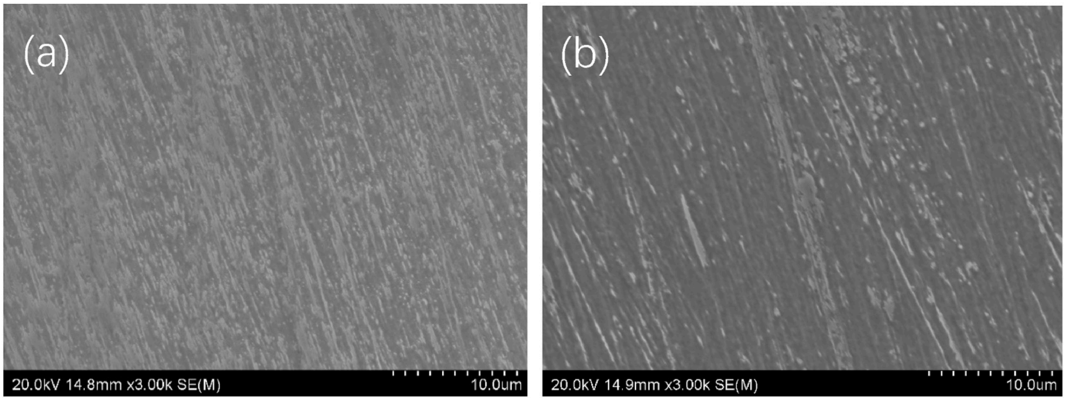

Fig. (12). SEM image of CP sample (a) and LP sample (b) after metallographic etching.

4. Conclusions

In this study, dry sliding wear tests were conducted on CP 718 and LP 718 alloy with Al_2O_3 counter balls at 2Hz, 5Hz and 8 Hz under 10 N,15 N and 20 N loads. The conclusions can be drawn as follows.

(1) Under identical working conditions, the wear rate of the LP material is a little higher than that of the CP material. After the friction process stabilizes, the coefficient of friction (COF) of the LP material also remains higher than that of the CP material during the initial 300 s.
(2) Both the CP and LP materials showed a clear increase in wear rate with increasing load, while no consistent trend was observed with respect to the experimental frequency. This can be explained by the competing contributions of multiple wear mechanisms operating under different frequency conditions.
(3) Microstructural analysis indicated that abrasive and adhesive wear, accompanied by slight oxidation, were the primary mechanisms on the worn surfaces of both CP and LP materials, the dominant causes of friction failure may vary, but the mechanisms are similar.
(4) The CP material exhibited limited delamination and good plasticity. The thickness of the plastically deformed layer decreased gradually with increasing load, while the debris quantity remained relatively low. By contrast, under higher loads, the LP material showed minimal delamination but a larger accumulation of debris. Brittle detachment of cellular-dendritic or columnar crystals led to flocculent structures, suggesting that oxidation and adhesive wear dominated the wear behavior of LP materials.

Declaration of competing interest

The authors declare that they have no known competing financial interests or personal relationships that could have appeared to influence the work reported in this paper.

Acknowledgments

This research was supported by the Professor Scientific Research Foundation of Hezhou University (HZUJS202206) and the Project of Central Fund for Guiding Local Scientific and Technological Development (Grant No. HEKE ZY2023008). Zhengxi Hu also would like to express his sincere gratitude to the Guangxi Education Department for providing financial support for his research on additive manufacturing at Auckland University of Technology.

References

[1] Hatami O, Adibi H, Rezaei SM. Application of a compressed air jet for cleaning of wheel surface in grinding nickel-based super alloy Inconel 718. CIRP J Manuf Sci Technol 2022;37:233–44.
[2] Gök MS, Küçük Y, Erdŏ gan A, Oge M, Kanca E, Günen A. Dry sliding wear behavior of borided hot-work tool steel at elevated temperatures. Surf Coat Technol 2017; 328:54–62.
[3] Döleker KM, Erdogan A, Yener T, Karaoglanlı AC, Uzun O, Gök MS, Zeytin S. Enhancing the wear and oxidation behaviors of the Inconel 718 by low temperature aluminizing. Surf Coat Technol 2021;412:127069.
[4] Wang R, Wang W, Zhu GL, et al. Microstructure and mechanical properties of the TiN particles reinforced IN718C composite. J Alloys Compd 2018;762:237–45.
[5] Wang W, Zhu GL, Wang R, et al. Novel in situ synthesized carbide reinforced Ni base composite for structural castings with high creep resistance. Mater Des 2019; 172:107711.
[6] Mostafaei M, Abbasi SM. Influence of Zr content on the incipient melting behavior and stress-rupture life of CM247LC nickel base superalloy. J Alloys Compd 2015; 648:1031–7.
[7] Rometsch Paul A, Zhu Yuman, Wu Xinhua, Huang Aijun. Review of high-strength aluminium alloys for additive manufacturing by laser powder bed fusion. Mater Des July 2022;219:110779.
[8] Marques Ana, Ângela Cunha, Mariana Rodrigues Silva at el. Inconel 718 produced by laser powder bed fusion: an overview of the influence of processing parameters on microstructural and mechanical properties. Int J Adv Manuf Technol 2022;121: 5651–75.
[9] Mageshwari Komarasamy a d, Shivakant Shukla a, Williams Sarah. Microstructure, fatigue, and impact toughness properties of additively manufactured nickel alloy 718. Addit Manuf August 2019;28:661–75.
[10] Hilaire Alexandra, Andrieu Eric, Wu Xinhua. High-temperature mechanical properties of alloy 718 produced by laser powder bed fusion with different processing parameters. Addit Manuf March 2019;26:147–60.
[11] Mandal Vijay, Sharma Shashank, Singh Sudhanshu S. Laser surface texturing in powder bed fusion: numerical simulation and experimental characterization. Met Mater Int 2022;28:181–96.
[12] Komarasamy Mageshwari, Shukla Shivakant, Williams Sarah. Microstructure, fatigue, and impact toughness properties of additively manufactured nickel alloy 718. Addit Manuf August 2019;28:661–75.
[13] Liu SY, Shao S, Guo H, et al. The microstructure and fatigue performance of inconel 718 produced by laser-based powder bed fusion and post heat treatment. Int J Fatig March 2022;156:106700.
[14] Li HY, Kong YH, Chen GS, et al. Effect of different processing technologies and heat treatments on the microstructure and creep behavior of GH4169 superalloy. Mater Sci Eng, A 2013;582:368–73.
[15] Popovich VA, Borisov EV, Popovich AA, Sufiiarov VS, Masaylo DV, Alzina L. Functionally graded Inconel 718 processed by additive manufacturing: crystallographic texture, anisotropy of microstructure and mechanical properties. Mater Des 2017;114:441–9.
[16] Firoz R, Basantia SK, Khutia N, et al. Effect of microstructural constituents on mechanical properties and fracture toughness of Inconel 718 with anomalous deformation behavior at 650 °C. J Alloys Compd 2020:845.
[17] Zhang Y, Lan L, Zhao Y. Effect of precipitated phases on the mechanical properties and fracture mechanisms of inconel 718 alloy. Mater Sci Eng, A 2023:864.
[18] Schneider Judy, Farris Laura, Nolze Gert, et al. Microstructure evolution in inconel 718 produced by powder bed fusion additive manufacturing. J Manuf Mater Process 2022;6:20.
[19] Amato KN, et al. Microstructures and mechanical behavior of Inconel 718 fabricated by selective laser melting. Acta Mater 2012;60(5):2229–39.
[20] Zou Yunhe, Tang Shufeng, Guo Shijie, Song Xiaojuan. Tool wear analysis in turning inconel-657 using various tool materials. Mater Manuf Process 2024;39(10): 1363–8. https://doi.org/10.1080/10426914.2024.2323434.
[21] Liu Kaiyuan, Zhang a Li, Cao Li, Wang Tiejun, et al. Binder jetting additive manufacturing of a 95W-3.5Ni-1.5Fe tungsten heavy alloy: enhanced ductility and

dynamic deformation mechanisms. Mater Sci Eng, A 2025;942:148719. https://doi.org/10.1016/j.msea.2025.148719.
[22] Lin Hao, Yin Xiaoping, Wang Ze, et al. Friction-induced PTFE coating on dental restorative resin with ultralow friction and wear. Langmuir 2025;41:22501–6. https://doi.org/10.1021/acs.langmuir.5c03007.
[23] Kocich Radim, Kunčická Lenka, Benč Marek, et al. Corrosion behavior of selective laser melting manufactured bio-applicable 316L stainless steel in ionized simulated body fluid. Int J Bioprint 2024;10(1):1416. https://doi.org/10.1016/j.corsci.2025.113221.
[24] Li Xiangyu, Zhao Yufan, Peng Yiqi, et al. Bulk single-crystal-like IN738 alloy fabricated using laser powder bed fusion by controlling the thermal flow. Mater Res Lett 2025;13(10):1072–9. https://doi.org/10.36922/ijb.1416.
[25] Chen Bo, Wang Shenqi, Li Wenying, et al. Investigation on the atomization mechanism of alloy powder by dual-gas nozzle and the powder defects formation. Powder Technol 2026;469:121768. https://doi.org/10.1080/21663831.2025.2563357.
[26] Zhao Yuhong, Zhang Bing, Hou Hua, et al. Phase-field simulation for the evolution of solid/liquid interface front in directional solidification process. J Mater Sci Technol 2019;35:1044–52. https://doi.org/10.1016/j.powtec.2025.121768.
[27] Zou Baoping, Chen Yu, Bao Yangjuan, et al. Impact of tunneling parameters on disc cutter wear during rock breaking in transient conditions. Wear 2025;560–561:205620. https://doi.org/10.1016/j.jmst.2018.12.009.
[28] Chen Yuqiang, Zimin HE, Heng LI, et al. Corrosion fatigue mechanisms and control technologies in aviation aluminum alloys:a critical review. Chin J Aeronaut 2026;39(2):103496. https://doi.org/10.1016/j.wear.2024.205620.
[29] Liu Yunfan, Zhu Lina, Ma Guozheng, et al. Tribocorrosion behaviours and mechanisms of Inconel 625–nano/microAl2O3 composite coatings prepared by plasma enhanced high-velocityarc spraying. Corros Sci 2025;256:113221. https://doi.org/10.1016/j.cja.2025.103496.
[30] Deng Dunyong, Peng Ru Lin, Brodin Håkan, et al. Microstructure and mechanical properties of Inconel 718 produced by selective laser melting: sample orientation dependence and effects of post heat treatments. Mater Sci Eng, A 2018;713:294–306.
[31] Hosseini a E, Popovich VA. A review of mechanical properties of additively manufactured Inconel 718 [19]. Addit Manuf 2019;30:100877.
[32] Xu Zhibiao, Li Dexiang, Lu Zhijie, Lv Xiaowen. Study on the damage evolution of fretting wear in an inconel 718 laser cladding alloy layer at different temperatures. Tribol Int January 2023;179:108092.
[33] Zahoor Ayna, Rahman Atikur, Butt Mohammad Mursaleen. Inconel 718 alloy: a study of microstructure, hardness, and tribological properties. Tribol Int 2025;210:110769.
[34] Li Hua, Ramezani Maziar, Chen Zhan Wen. Dry sliding wear performance and behaviour of powder bed fusion processed Ti–6Al–4V alloy. Wear 2019;440–441:203103.
[35] Chintha AR. Metallurgical aspect of steels designed to resist abrasion, and impact abrasion wear. Mater Sci Technol 2019;35(10):1133–48.
[36] Qiu X, Wei X, Xu X, et al. Dependence of fretting wear resistance on microstructural features of alloyed steels. Tribol Int 2019;137:39–45.
[37] Chintha AR, Valtonen K, Kuokkala VT, et al. Role of fracture toughness in impact-abrasion wear. Wear 2019;428–429:430–7.
[38] Xu Ruiwen, Zhu Yi, Wu Jianxiong, et al. Hybrid high-temperature wear mechanisms of additive manufacturedTi-6Al-4V alloy. Tribol Int 2025;205:110559.
[39] Camus DE, Jaramillo RA, Plyburn JA, Suarez FS. Evolution of microstructure during hot rolling of Inconel 625 and 718[J]. The minerals. Metals & Materials Society; 1997. p. 291–302.
[40] Sui Feng-li, Zuo Yue, Liu Xiang-hua, Chen Li-qing. Microstructure analysis on IN 718 alloy round rod by FEM in the hot continuous rolling process. Appl Math Model 2013;37:8776–84.
[41] Lawitzki R, Hassan S, Karge L, Wagner J, Wang D, Kobylinski JV, Krempaszky C, Hofmann M, Gilles R, Schmitz G. Differentiation of γ'- andγ''-precipitates in Inconel 718 by a complementary study with small-angle neutron scattering and analytical microscopy. Acta Mater 2019;163:28–39.
[42] An XL, Zhang B, Chu CL, Zhou L, Chu PK. Evolution of microstructures and properties of the GH4169 superalloy during short-term and high-temperature processing. Mater Sci Eng A 2019;744:255–66.
[43] Dongyang Hao, Jin Wanjun, Ma Haikun. Microstructure evolution and creep behavior of Inconel 718 alloy subjected rolling process. Mater Char 2025;223:114888.
[44] Anandakrishnan V, Sathish S, Muthukannan Duraiselvam. Dry sliding wear behavior of Inconel 718 additively manufactured by DMLS technique. Ind Lubric Tribol 2020;72(4):491–6.
[45] Li Hua, Ramezani Maziar, Li Ming, Ma Chao. Jyhwen Wang tribological performance of selective laser melted 316L stainless steel. Tribol Int 2018;128:121–9.